Materials Characterization 151 (2019) 84–95

Contents lists available at ScienceDirect

Materials Characterization

journal homepage: www.elsevier.com/locate/matchar

Variation of microstructural features on the tensile property and corrosion resistance of Zr-Sn-Nb-Fe-Cu alloy

Huigang Shi[a], Xianglong Guo[b], Jiuxiao Li[c], Jianwei Mao[a], Junqiang Lu[d], Weijie Lu[a,*]

[a] *State Key Laboratory of Metal Matrix Composites, School of Material Science and Engineering, Shanghai Jiao Tong University, Shanghai 200240, PR China*
[b] *School of Nuclear Science and Engineering, Shanghai Jiao Tong University, No. 800 Dongchuan Road, Shanghai 200240, PR China*
[c] *School of Materials Engineering, Shanghai University of Engineering Science, Shanghai 201620, PR China*
[d] *Shanghai Nuclear Engineering Research and Design Institute Co., Ltd., Shanghai 200233, PR China*

ARTICLE INFO

Keywords:
Zirconium alloy
β-Quenching
Microstructure
Yield phenomenon
Work hardening
Corrosion resistance

ABSTRACT

Zr-Sn-Nb-Fe-Cu alloy was processed by two kinds of heat treatment and different microstructures were obtained. We focus on the effect of microstructure variation on the tensile properties and corrosion resistance. Results found that all specimens annealed at 550 °C/5 h (group A) could induce complete recrystallized structure, while dislocation cells and sub-grains formed after β-quenching and subsequent annealing at 480 °C/5 h (group B). Meanwhile, the average size and density of second phase particles (SPPs) for group A were slightly higher than that for group B. The tensile test results indicated that the yield phenomenon with distinct upper and lower yield points in tensile curves is observed due to the complete recrystallized structure with little dislocations in group A. For group B, however, the direct work hardening behavior was obtained at the initial deformation due to the interaction of existing dislocations with GBs and SPPs. The samples in group B showed a significant improvement in yield strength (YS), with a medium loss in plasticity compared with that for group A. The multiple strengthening contributions to YS mainly originate from the combination of grain refinement and dislocation. Theoretical analysis results found that the dislocation strengthening exhibited a significant effect on the tensile properties. Autoclave corrosion test indicated the specimens for group B possessed a relatively worse corrosion resistance. It was attributed to the higher O ion diffusion rate in defects and more vacancies or dislocations produced in the oxide of group B.

1. Introduction

Zirconium alloy cladding tubes are widely served as structural materials in nuclear power reactors due to their excellent corrosion resistance, superior mechanical properties and low neutron absorption rate [1–3]. The corrosion resistance of these materials is one of the crucial factors in the serve life limitation of fuel assemblies. With trends towards increasing burn-up [4] and utilization of in-reactor bred fuel [5], great efforts have been made to develop new zirconium alloys with advanced corrosion resistance during the past several decades [6–8]. It is well known that adjusting chemical compositions can optimize the performance of zirconium alloys. For instance, Lee [9] reported that the addition of 160 ppm P could both improve the mechanical strength and ductility of Zr-1.5Nb-O alloy. Charquet [10] also reported that trace S had a beneficial effect on the creep strength and steam corrosion resistance of Zr—S alloy at 400 °C. Yang [11] presented that doping of Mo (0.1–0.7wt%) greatly retarded the recrystallization process and significantly reduced the grain size in Zr—Nb alloys. In parallel, the mechanical properties and corrosion resistance of zirconium alloys are controlled by the thermo-mechanical processing. For example, Sahoo [12] reported that after 50% plane strain deformation the un-deformed grains are still obtained in Zr-2 and the heterogeneous deformation contributed to the uneven distribution of residual stresses. Jiang et al. [13] demonstrated that homogeneous, equiaxed ultrafine grains (UFG), with average size of 400 nm, could be obtained after two accumulative roll bonding (ARB) cycles for pure Zr. The YS and ultimate tensile strength (UTS) were nearly double that of conventionally processed Zr. Panicaud [14] investigated that a nano-crystallisation treatment has a beneficial effect on the corrosion resistance of M5 alloy at 550 °C in artificial air.

It is generally accepted that β-quenching in the manufacturing processes of zirconium alloys is a crucial step in controlling the properties of the final products. For instance, Yao et al. [15] found that Zr-4 treated by β–quenching exhibited excellent corrosion resistance in

---

[*] Corresponding author.
E-mail address: luweijie@sjtu.edu.cn (W. Lu).

https://doi.org/10.1016/j.matchar.2019.02.043
Received 23 November 2018; Received in revised form 28 February 2019; Accepted 28 February 2019
Available online 01 March 2019
1044-5803/

lithiated water with 0.01 M LiOH, which was attributed to the increase of supersaturated solid solution contents of Fe and Cr in α-Zr matrix. Chen et al. [16] investigated the effect of β-quenching on the performance of corrosion resistance and hydrogen pick-up capability. They found that after β-quenching the samples exhibited better corrosion resistance and lower hydrogen pick-up. However, there is still a lack of clear investigation on the microstructure variation, tensile properties and corrosion behaviors of zirconium alloys, which subjected to β-quenching and subsequent annealing.

Hence, it is necessary to study the tensile properties and corrosion behavior of zirconium alloy with different heat treatment, especially treated by β-quenching and subsequent annealing. In this work, a new zirconium alloy (Zr-0.5Sn-0.4Nb-0.3Fe-0.05Cu) is prepared by two kinds of heat treatment. One is annealed at 550 °C for 5 h, and the other one is β-quenched and annealed at 480 °C for 5 h. The microstructure and tensile properties of the experimental alloys are characterized. Furthermore, corrosion tests in autoclave are performed up to 300 days to evaluate the corrosion resistance of the materials.

2. Experimental procedure

2.1. Material preparation

The composition of the Zr-Sn-Nb-Fe-Cu alloy used was listed in Table 1. The as-received samples were prepared by a sequence of vacuum arc re-melting for three times to ensure the chemical homogeneity of materials. The disk-shape ingots were forged to 10 mm thick at 1000 °C and then β-solution treated at 1050 °C for 30 min before being quenched in water. Then a serial of hot rolling were conducted at 650 °C for 1 h to the thickness of 4.7mm, followed by cold rolling to 1.8mm thick with two intermediate heat treatments at 550 °C for 4 h. The as-received samples were divided into two groups (denoted as group A and B), and the processing routes for each group were depicted schematically in Fig. 1. For group A, two times of annealing were conducted at 550 °C for 4 h with two intermediate cold rolling to 0.65 mm final thick. After final cold rolling, samples were annealed at 550 °C for 5 h. In contrast, the β-quenching processing was carried out in group B, then the samples were cold rolled to 0.65 mm. The intermediate annealing treatment and the final annealing treatment were 500 °C for 4 h and 480 °C for 5 h, respectively.

2.2. Microstructure characterization

The microstructure of the materials was observed by using a JEOL 7800F field emission gun scanning electron microscope (SEM) and a JEOL 2100F transmission electron microscope (TEM) equipped with an energy dispersive X-ray spectroscopy (EDS) detector. The samples for SEM observations were polished according to standard metallographic techniques and then etched in a hybrid solution containing H_2O: HNO_3: HF of 9: 9: 2 for about 20s. The distribution information of SPPs' sizes was obtained by the Image-Pro Plus 6.0 software from the SEM images with a magnification of 10,000×. To ensure the reliability of the statistical results, at least 500 particles and 20 photos from each sample were counted. A gold layer sputtered to the oxide cross-sectional specimens was used to improve the surface conductivity. The specimens for TEM observations were prepared using a twin-jet polishing with a mixed solution (C_2H_5OH:$HClO_4$ = 9:1) at a voltage of 30 V and a temperature of −30 °C. EBSD measurements were performed with an AZtec HKL Max system, installed on a Mira 3 SEM scanning electron microscope. EBSD data for each sample were collected at step size of 0.1μm with a scanning area of 90 × 130um^2 on the surface determined by rolling direction (RD) and normal direction (ND). The cross-sectional samples of the oxides for TEM observation were prepared using a FEI Scios focused ion beam (FIB) in situ lift-out technique [17]. The surface of oxide was protected with a Pt layer with a thickness of 1 μm by thermal evaporation on the surface of the specimen corroded for 100 days in order to protect the initial surface and make the oxide conductive. Then the sample was tilted with its surface perpendicular to the ion beam. Trenches were milled on three sides of the TEM specimen, starting with 6.5nA and reducing the current to 1.5nA near the deposited strip. The TEM specimen was thinned from both sides by milling with ion beam currents from 750pA down to 80pA with the specimen tilted up to 1–2° off the ion beam direction to obtain as parallel sides as possible. Finally, the TEM lamella was obtained by milling with 60pA beam current on the thinned region to remove the amorphous layer formed by the higher energy ion milling.

Table 1
Chemical composition (in wt%) of the materials studied in this work.

Alloy	Element				
	Zr	Sn	Nb	Fe	Cu
Zr-Sn-Nb-Fe-Cu	Bal.	0.49	0.43	0.28	0.047

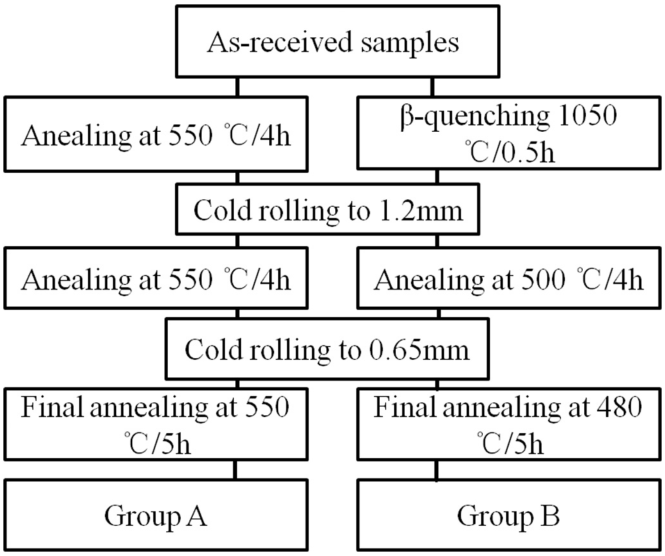

Fig. 1. Schematics of heat treatment history of experimental alloy for both groups.

2.3. Tensile properties

Dog-bone flat tensile coupons of 20 mm gauge length and a cross section of 12 mm × 0.6mm were machined out of the alloy samples by electric discharge machining. Room temperature tensile tests were carried at 1×10^{-3}/s in a Zwick Z100/SN3A universal testing machine. The tensile axis was set to be parallel to the rolling direction. Afterward, the samples were mechanically ground with SiC paper up to 2000 grits. After the tensile test, the fracture surface of the specimens was observed by a conventional SEM.

2.4. Autoclave corrosion

Samples used for autoclave corrosion testing were 25 mm × 15 mm × 0.6mm in size and chemically polished using a pickling solution (10% HF, 30% HNO_3, 30% H_2SO_4 and 30% H_2O, in volume). Then the specimens were sequentially rinsed in pure water, boiling deionized water and then blow-dried with warm air. The corrosion experiments were conducted in a static autoclave containing deionized water at 360 °C/18.6MPa. The corrosion behavior was evaluated by weight gain per unit area as a function of exposure time, such as 3, 14, 42, 70, 100, 130, 160, 200, 260 and 300 days.

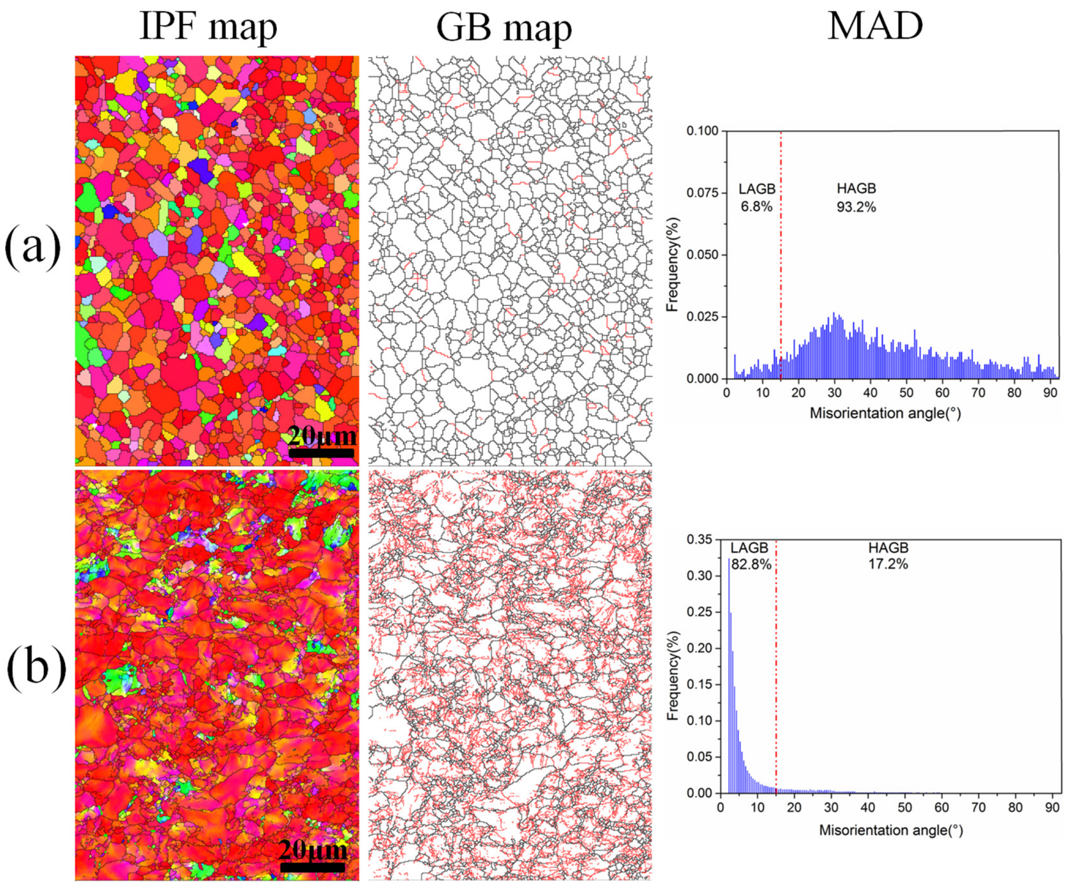

Fig. 2. EBSD IPF maps, GB maps and MAD histograms of samples for (a) group A and (b) group B.

3. Results

3.1. Characteristics of microstructure and precipitates of the specimens

To reveal microstructure features of two group samples after final annealing, EBSD examinations are firstly performed. Fig. 2 shows the inverse pole figure (IPF) maps, grain boundary (GB) maps and misorientation angle distribution (MAD) histograms derived from EBSD data sets for two group samples. From the IPF maps, it can be observed that the microstructure for group A is composed of equiaxed grains with relatively uniform size, implying that the complete recrystallization is achieved in group A. By contrast, it is noted that the microstructure for group B is almost completely dominated by irregular grains, namely large deformed grains surrounded by lots of fine grains. In regard to the GB maps, it should be noticed that high angle grain boundaries (HAGBs, misorientations higher than 15°, marked as black line) are predominant over low angle grain boundaries (LAGBs, misorientations lower than 15°, marked as red line) for group A, while obviously opposite result is observed for group B, in which most of the grains are indeed sub-divided into several parts separated by many LAGBs. This significant discrepancy between these two groups can also be observed in MAD histograms by a quantitative measurement. For group A, only 6.8% LAGBs possesses the total GB map, while the primary misorientation angle is around 30°. This similar characteristic is commonly reported by other researchers in rolled and recrystallized Zr alloys, corresponding to their specific texture [18,19]. On the contrary, the fraction of LAGBs for group B is almost 82.8%, overwhelmingly higher than that of HAGBs (17.2%).

Fig. 3 illustrates the grain size distribution and the recrystallized fractions of grains for the two groups. It is worth noting that grain size in group A ranges from 1.1μm to 11.6μm, and the average grain size is 3.3μm (Fig. 3a). The grain size in group B, however, ranges from 0.4μm to 14.4μm, and the average grain size is only 1.5μm (Fig. 3b), which is significantly lower than that of group A. In this regard, the highly irregular grain shape, combined with predominantly large fraction of LAGBs in group B, indicated that the microstructure in group B is still far from equilibrium recrystallization. The recrystallized fractions of grains for both two groups are presented in Fig. 3c. Obviously, the recrystallization fraction is 96.5% for group A, overwhelmingly higher than that of group B (only 7.2%). This phenomenon further demonstrates that samples in group A have a fully recrystallized structure, while samples in group B are still on the initial stage of recrystallization. As also noted in Fig. 3c, the sub-structured fraction and deformed fraction are 1.2% and 2.3% for group A, while these values are 43.5% and 49.3% for group B, respectively. This indicates that microstructure of group B is almost completely dominated by sub-grains and deformed grains, which should be attributed to grain subdivision caused by dislocation slip.

Fig. 4 exhibits the TEM micrographs of both groups. After the final annealing (550 °C/5 h) the recrystallization is completed in group A. As shown in Fig. 4a, the microstructure is typically composed of equiaxed grains and dispersive precipitates. The well-equiaxed grain size is 3–5 μm, and dislocations can hardly be observed, in accordance with the EBSD results. By contrast, a great number of dislocation cells are detected and many sub-grains with size less than 500 nm are also found in group B, as shown in Fig. 4b. The dislocation cells contain high density of dislocations, which are stacked in the vicinity of GBs, indicating that their moving is strongly impeded by GBs. The co-existence of dislocation cells and sub-grains further reveals the samples in group B are still on the early stage of recrystallization.

With respect to the second phase particles (SPPs), the morphologies and distributions of the SPPs in both groups are examined. As

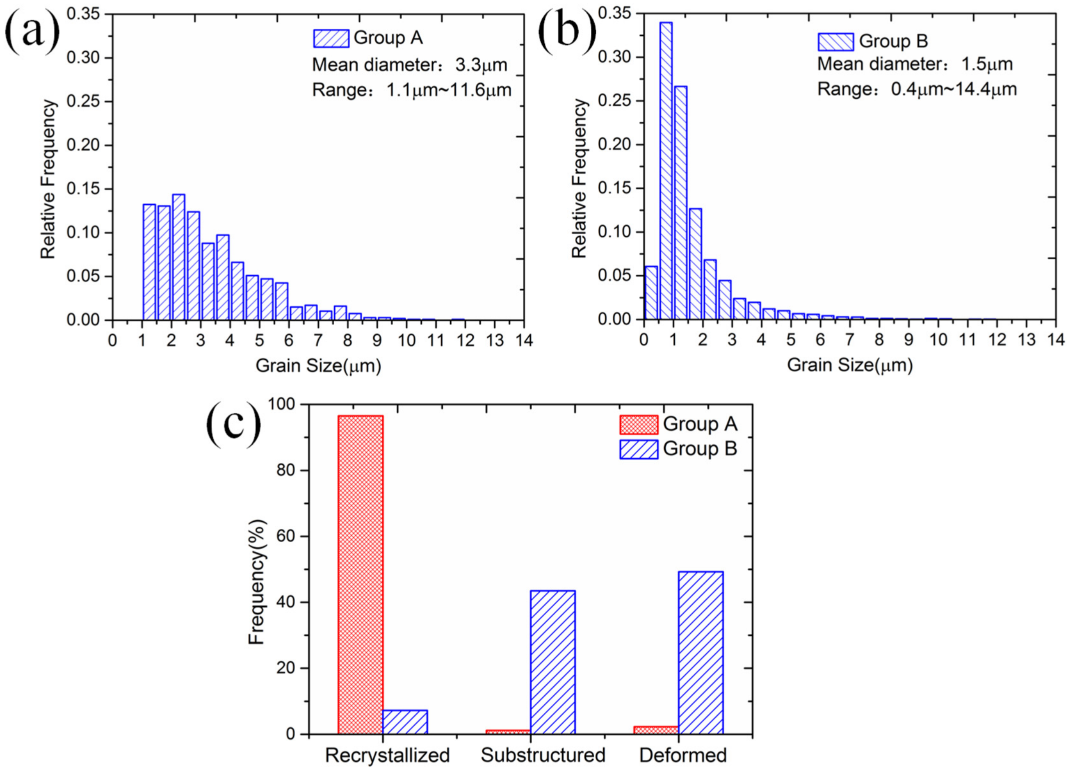

Fig. 3. (a) and (b) grain size distribution of specimens derived from EBSD examination for group A and group B, respectively. (c) Recrystallized, sub-structured and deformed fractions of specimens derived from EBSD data for both group.

illustrated in Fig. 5a and b, the SPPs in both groups situate along the grain boundary (denoted by the white arrows) and in grain interior, with a random distribution. The SPPs' shapes are almost sphere or ellipsoid. In addition, the density of SPPs in group A is slightly higher than that in group B. A quantitative measurement is used. At least 500 particles are counted to ensure the data reliability. As represented in Fig. 5c and d, the size of the SPPs ranges approximately from 50 nm to 300 nm and the main size is 100–150 nm in all the samples. The average size and volume fraction of the SPPs are almost 132 nm and 2.5% in group A, while these values are about 124 nm and 1.7% in group B, which are slightly lower than those in group A. The reason for this can be attributed to the β-quenching and relatively low final annealing temperature for group B.

Fig. 6 presents the TEM observations of SPPs in both groups. The crystal structure of SPP is examined by selected area electron diffraction (SAED) analyses. It is worth noting that many dislocation lines can be found in the interior of grains in group B (Fig. 6e and g), while dislocation line can hardly be observed in group A (Fig. 6a and c). As shown in Fig. 6b and d, the SAED patterns identify the SPPs as $(Zr, Nb)_2Fe$ with FCC crystal structure and $Zr (Nb, Fe)_2$ with HCP crystal structure for group A, respectively. The same results are observed in group B (Fig. 6f and h, respectively). Fig. 7 presents the typical EDS spectrum of the analyzed SPPs in both groups. Results show that for the SPPs with FCC crystal structure, the detailed chemical composition (in at.%) of the SPPs are (52–69.2)Zr-(1.5–8.8)Nb-(23.5–37.8)Fe-(3.5–7.8)Cu. For the SPPs with HCP crystal structure, the detailed chemical composition of the SPPs are (33.3–34.5)Zr-(30.7–32.6)Nb-(24.3–27.5)Fe-(1.5–3.6)Cu. The content of Cu in both types of SPPs is less than 8% in all investigated SPPs analyzed by EDS. Note that Cr was detected as an impurity in the SPPs because Cr is not a nominal alloying element in our alloy.

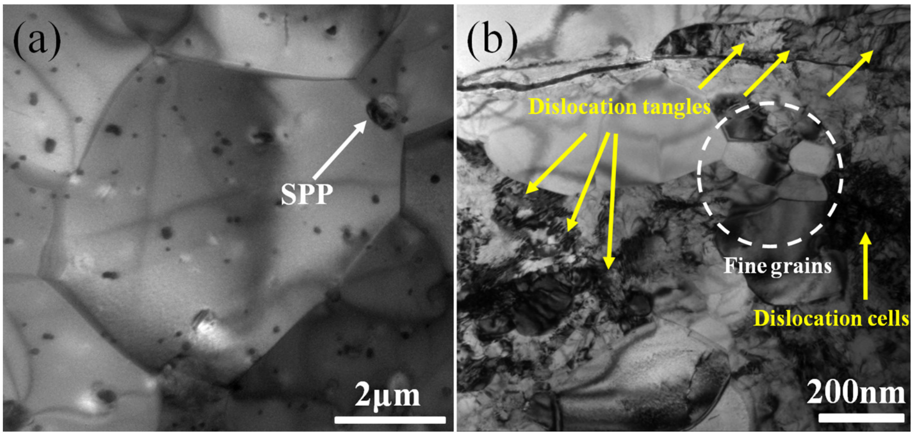

Fig. 4. TEM micrographs of specimens of (a) group A and (b) group B.

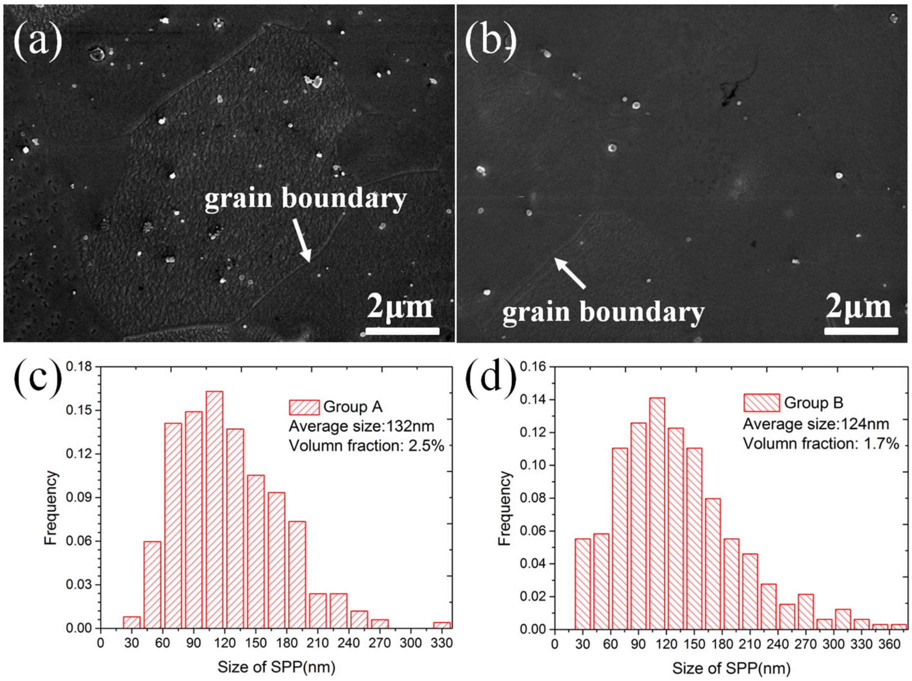

Fig. 5. SEM micrographs showing the SPPs and the grain boundaries of samples in (a) group A and (b) group B. (c) and (d) are the size distribution of SPPs measured by SEM images in group A and group B, respectively.

3.2. Tensile properties

Fig. 8 demonstrates the true stress-strain curves for group A and B. The tests are performed at room temperature and at a strain rate of 10^{-3}/s. For group A, it is interesting to note that clear yield phenomenon with apparent upper and lower yield points can be observed (inset image in Fig. 8). This phenomenon is usually observed in low carbon steels, and is commonly attributed to formation of Cottrell atmosphere [20]. This has not been reported so far in conventionally processed zirconium alloys and is strongly correlated with the microstructure of specimens. The reason for this phenomenon will be discussed in detail in Section 4.2. With increasing strain, work hardening is exhibited after the load drop in group A and the work-hardening rate Θ decreases. The YS and UTS for group A are, respectively, 416 MPa and 622 MPa. For group B, the load drop is not observed and direct work hardening is obtained after yield. The specimens in group B exhibit significantly higher YS and UTS, namely 539 MPa and 704 MPa, respectively. Simultaneously, it can be seen that group B has remarkably lower elongation (23.8%) than group A (33.5%). The tensile properties are summarized in Table 2. The reasons accounting for these discrepancies can be attributed to sub-grains and dislocation cells in group B, while the well-equiaxed grains with complete recrystallization in group A, and will be discussed in Section 4.2.

Fig. 9 shows the cross-sectional tensile fractographs of the samples in both groups. The fracture surface of group A consists of large and deep dimples, revealing splendid plasticity in this sample. In group B, nevertheless, similar characteristics with relatively smaller and shallower dimples are observed, which indicates the ductility of group B is not as good as that of group A.

3.3. Corrosion resistance and oxide cross-sectional microstructure

Fig. 10 reveals the oxidation kinetic of the samples in deionized water, determined by measuring the weight gain that results from oxygen ingress. During the first 200 exposure days, both groups have almost the same features in the curves, and the oxidation kinetic initially follows a parabolic type [21,22] progression. A dramatically accelerated oxidation rate is observed after 200-day exposure in group B, indicating the transition occurred from one oxide period to the next. As for group A, there is no evident increment in weight gain until 260-day exposure. Thus, we can conclude that the first oxidation transition time for group A and B are almost 260 days and 200 days, respectively, and group A possesses a relatively better corrosion resistance than group B.

To further characterize the oxidation behavior in detail, micrographs of the oxide/metal cross-section are shown in Fig. 11. At exposure time of 100 days, as shown in Fig. 10a and e, both large columnar grains and smaller equiaxed grains are clearly observed in the oxide films formed on the two groups. The equiaxed grains are more prevalent in the vicinity of the oxide/water interface, while the columnar grains are located in the inner part of oxide film, aligns in the oxide growth direction and growing perpendicular to the oxide/metal (O/M) interface. With up to 200 days, several lateral cracks can be found mainly parallel to the O/M interface, and a few micro-voids are observed in the outer part of oxide film near the equiaxed grains, as seen from Fig. 11b and f. It should be noted that, the oxide film in group B has more cracks, and some of these cracks link together to form a long crack, resulting in the formation of two layers, which imply that oxidation transition already occurred before 200 days. As exposure time increases to 260 days, one can see that oxide films in both groups is divided by long and undulated cracks, and a multiple layer structure is observed (Fig. 11c and g). The only discrepancy between them is that the inner layer of oxide film in group B is thicker than that of group A, while the outer layer has almost the same thickness. These similar characteristics could also be observed in the samples with 300-days exposure (Fig. 11d and h).

The detailed information about oxide films is listed in Table 3. A layer of equiaxed grains is 300–500 nm in thickness, and the columnar grains are 300–700 nm in length and 50–100 nm in width. At 100-day exposure, the thickness of the oxide film is 2.1–2.5μm for both group A and B. However, with exposure time being increased to 200 days, a relatively thicker oxide film is obtained on group B than that on group A, indicative of a worse corrosion resistance of group B.

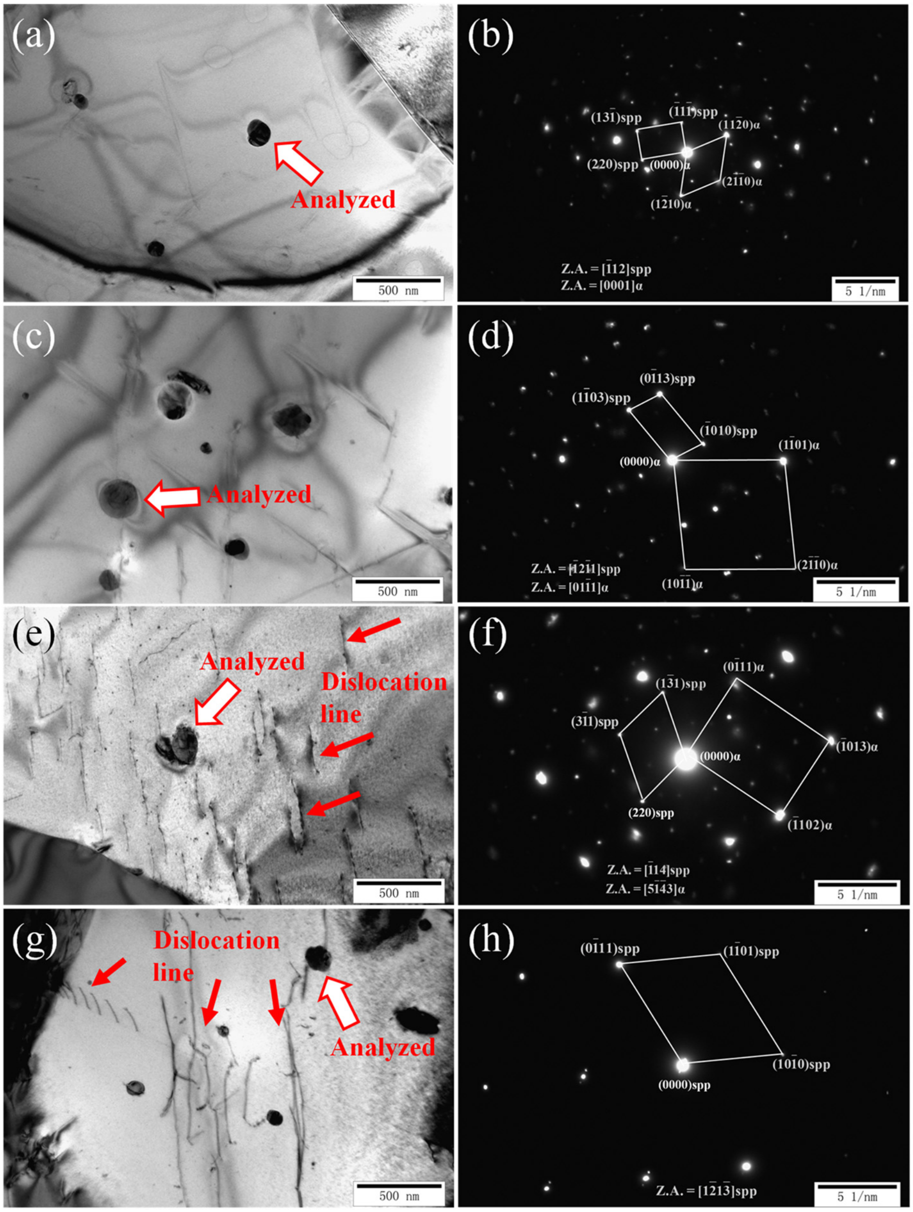

Fig. 6. TEM bright filed image of the analyzed SPPs for specimens: (a–d) group A; (e–h) group B. The corresponding electron diffraction patterns of the analyzed SPPs for group A and B show that there are two types of SPPs: FCC (Zr, Nb)$_2$ Fe and HCP Zr (Nb, Fe)$_2$.

4. Discussion

4.1. Effect of heat treatment on microstructural morphology

It has been well documented [23,24] that after β-quenching, the β phase has transformed into interlaced α-plate structure, which shows straight interface and arranges parallel to each other. High density of defects such as dislocations and vacancies possess in α-lath martensite, leading to high energy in the system. In general, the large reduction by repeated cold rolling is believed to induce sufficiently high density of dislocations [25], which tangle together [14], or array in lamella structure [14], and finally become dislocation cells.

Additionally, majority of the grains are fragmented by dislocation slip. During the annealing process, these dislocation cells develop into sub-grains, and further coalesce together by grain boundaries movement and dislocations slip, resulting in the recrystallization nucleation behavior. These sub-grains continue to grow up towards the deformed region by the boundaries migration until entire well-equiaxed grains form. Note that β-quenching and relatively low annealing temperature are performed in the samples of group B, the recrystallization does not accomplished, or even maintains at the initial stage. The sub-grains have not enough time or sufficient energy to merge together by dislocations slip or annihilation, resulting in the conservation of dislocations and sub-grains that generated in the cold rolling process. As demonstrated in Fig. 12, a considerably high density of dislocations aggregate near the grain boundary, and some of them tangle or form cells. The specimens in group B are at the initial stage of recrystallization with sub-grains less than 500 nm as well as high density of dislocations co-exist, as shown in Fig. 4b. This phenomenon can also be confirmed by EBSD observation. Large fraction of LAGBs (~82.8%) and extremely low recrystallization fraction (~7.2%) is observed in group B. On the contrary, samples in group A possess completely recrystallized microstructure. The well-equiaxed α-grains, combined with remarkably fraction of HAGB (93.2%) and predominantly recrystallization fraction (96.5%) can be observed by TEM and EBSD images. Another phenomenon one should notice is that the average size

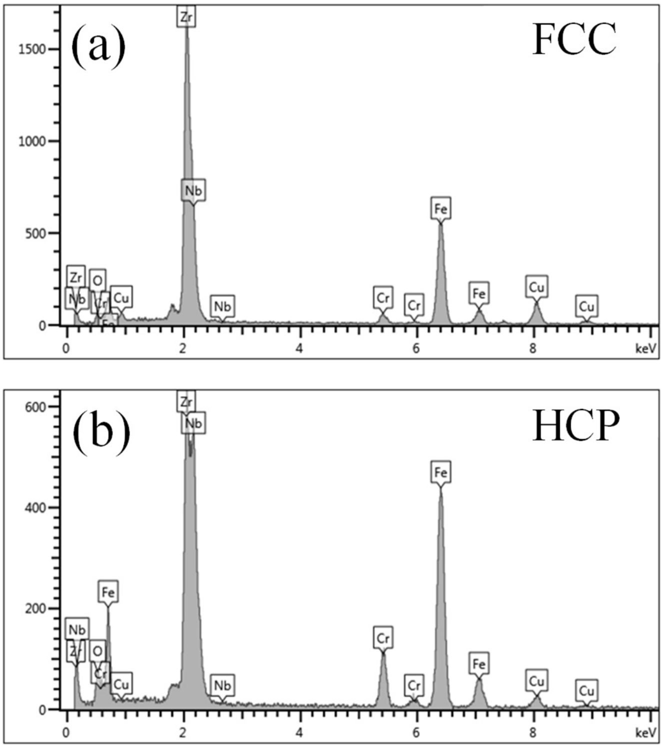

Fig. 7. The typical EDS spectrum of the analyzed SPPs for the (a) FCC structure and (b) HCP structure.

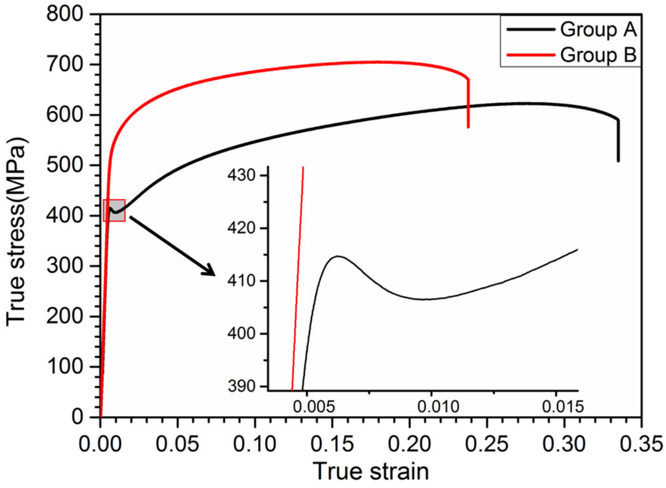

Fig. 8. The tensile stress-strain curves of specimens in both groups at room temperature.

Table 2
Mechanical properties of alloy in air at room temperature.

Alloy	YS (MPa)	UTS (MPa)	Elongation (%)
Group A	416 ± 11	622 ± 8	33.5 ± 1.1
Group B	539 ± 10	704 ± 5	23.8 ± 0.4

and volume fraction of SPPs in group B (124 nm and ~1.7%) is slightly lower than in group A (132 nm and ~2.5%). During annealing, accompanied by recrystallization, those supersaturated alloying elements after β-quenching precipitate as SPPs to minimize the system's energy. For specimens in group B which has just recrystallized, the SPPs are inadequately precipitated, and rarely have time to grow up, resulting in the lower values of SPPs' average size and volume fraction. All these differences on matrix microstructure and SPPs between two groups could exert a significant influence on the mechanical properties, which will be discussed in the next section.

4.2. Effect of microstructural feature on tensile properties

As mentioned above, the yield phenomenon is observed in group A, while no load drop is obtained in group B. It is well known that a Cottrell atmosphere is formed by the segregation of impurities round dislocations in low carbon steels [20]. When the impurities congregate together, they act as particles that then impede dislocation motion, and higher stresses are needed to unpin them from the Cottrell atmosphere. Once these dislocations become free, the corresponding stress is reduced, and a load drop is observed [26]. In our samples, it is likely possible that the solute atoms are attracted to the strain field surrounding stationary dislocations and such dislocations need an extra shear stress to initiate dislocations move away from the solute atoms. However, load drop is not found in group B, even though there are lots of dislocations and solute atoms (such as Sn, Nb, Fe or Cu) existed in it. Thus, the theory of Cottrell atmosphere would be not suitable for our alloy.

According to the dislocation theory [27], the strain rate $\dot{\varepsilon}_p$ of materials during deformation are proportional to mobile dislocation density ρ_m in the crystals, the average velocity of dislocation ν, and the Burgers vector b of dislocations. Thus it can be written as follows:

$$\dot{\varepsilon}_p \propto \rho_m \cdot v \cdot b \tag{1}$$

and the average velocity v can be expressed as

$$v = \left(\frac{\tau}{\tau_0}\right)^{m'} \tag{2}$$

where τ_0 is the stress required for dislocation to move at unit velocity, τ is the effective shear stress acting on the dislocation, and m' is the stress sensitivity index and is related to materials. During the tensile test, $\dot{\varepsilon}_p$ is determined by the speed of extensometer chuck and is close to a constant (10^{-3} in our test). As shown in Fig. 4a, little dislocation existed in the interior of the microstructure before tension test in group A. So the mobile dislocation density is very low in the crystal. To maintain the constant value of $\dot{\varepsilon}_p$, we must increase the value of ν, therefore the value of τ must be increased and this value corresponds to the upper yield point. Once the plastic deformation begins, the dislocations proliferate rapidly and the value of ρ_m increases quickly. The value of ν must decrease quickly due to the constant value of $\dot{\varepsilon}_p$. So the value of τ also drops abruptly and this value corresponds to the lower yield point. As the plastic deformation continues, the increasing density of dislocations result in more dislocations plugged at the GBs and SPPs. The required stress gradually increases and work hardening behavior occurs. When the work-hardening rate Θ becomes negative, the stress decreases with increasing strain, which is called strain-softening behavior [28]. This phenomenon in tensile tests can be attributed to the occurrence of necking [29], and then the specimen fractured.

For group B, the microstructure comprises of lots of dislocations and SPPs. The stress curve exhibited direct work hardening at the early stage of deformation due to the interaction of dislocations with GBs and SPPs. The early work hardening in group B will lead to the decline of plasticity. Compared with group A, the YS of group B increases by about 123 MPa. The multiple strengthening contributions to the YS mainly originate from the combination of grain refinement, dislocation and SPPs. To further elucidate the relationship between microstructure and the corresponding mechanical property, the strength enhancement model is established to quantitatively demonstrate the effect of the various factors on the YS of group B.

According to the Hall-Petch relationship [30], the GB strengthening can be expressed as the following:

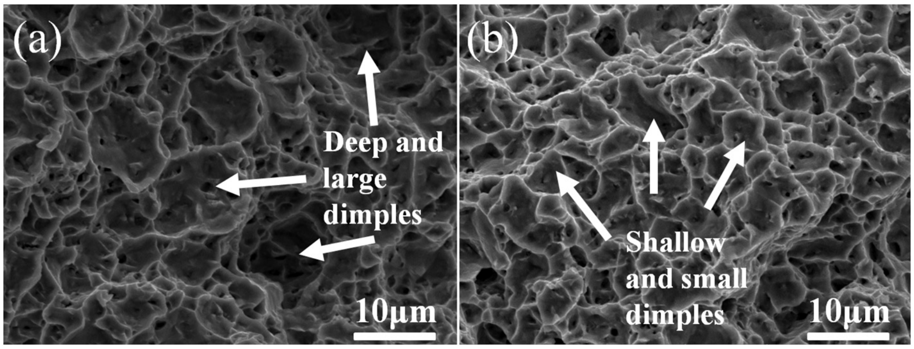

Fig. 9. SEM micrographs of the fracture surface for (a) group A and (b) group B.

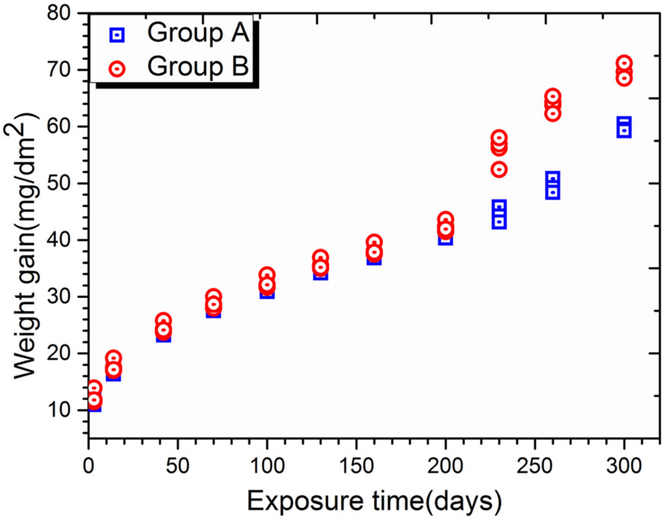

Fig. 10. Autoclave oxidation weight gain curves for both groups in deionized water at 360 °C/18.6MPa during 300 days exposure.

$$\Delta\sigma_{gb} = \Delta\left(\frac{k_{gb}}{\sqrt{D}}\right) \tag{3}$$

where k_{gb} and D are the material constant and the average grain size, respectively. Here the value $k_{gb} = 200\,\mathrm{MPa}\,\mu\mathrm{m}^{1/2}$ in pure Zr [31] is used.

The dislocation strengthening is commonly evaluated with the classic equation in the models [32]:

$$\Delta\sigma_{dis} = M\alpha Gb\sqrt{\Delta\rho_{dis}} \tag{4}$$

where M is the Taylor factor which is derived from the raw EBSD data (3.06 for group A and 2.93 for group B), α is the interaction strength between dislocations and ranges from 0.25 to 0.4 [33,34] as shown in previous studies. Here $\alpha = 0.25$ is used for approximate calculation in order to make the result of calculation close to the experimental data. G is shear modulus of Zr, and its value varies from 33GPa to 40GPa for Zr in different studies [11,25,34]. Here we use $G = 36.7$GPa [25] for approximate calculation. b is the magnitude of the Burgers vector of dislocations in zirconium (0.3 23 nm for the prism $\{10-10\}\langle 11-20\rangle$, which is the main slip system in α-Zr [35]) and ρ_{dis} is the dislocation density. In general, LAGBs in metals or alloys are commonly composed of a series of parallel or vertical edge dislocations or intersected screw dislocations, such as sub-grain boundaries and tilted grain boundaries. Based on our previous analysis in Section 3.1, for group B, lots of dislocations tangle to form cells and sub-grains, and store in LAGBs, thus the dislocation density ρ_{dis} here could be estimated by [36]

$$\rho_{dis} = \rho_0 + \rho_{LAGB} \tag{5}$$

in which ρ_0 is the dislocation density between boundaries and can be neglected owing to its small value; ρ_{LAGB} is the dislocation density accumulated in LAGBs that can be expressed as

$$\rho_{LAGB} = \frac{3\theta_{AV}^{LAGB} f_{LAGB}}{bD} \tag{6}$$

in which f_{LAGB} is the fraction of LAGBs; $\theta_{AV}{}^{LAGB}$ is the average boundary misorientation angle of LAGBs and D is the average grain size.

Substituting Eq. (6) into Eq. (4) gives

$$\Delta\sigma_{dis} = M\alpha G\sqrt{3b\square\left(\frac{\theta_{AV}^{LAGB} f_{LAGB}}{D}\right)} \tag{7}$$

The strengthening effect of SPPs in matrix can be attributed to the Zener pinning effect [37]. As shown in Fig. 13, the dislocations are accumulated in the vicinity of SPPs, implying they apparently impede the dislocations' movement. The pinning effect of SPPs in both groups can be expressed as [38]

$$\Delta\sigma_{spp} = M\alpha' Gb\Delta\left(\sqrt{N_{SPP} d_{SPP}}\right) \tag{8}$$

where α' is the obstacle strength of particles embedded in Zr matrix and a factor of 0.8 is used because the SPPs in zirconium alloys are impenetrable against dislocation advancing [39], M, G and b have the same significance as above, N_{spp} and d_{spp} are the number density and average size of particles in matrix.

When several strengthening effects are presented simultaneously, Ramakrishnan's approach [40] can be employed to calculate the YS:

$$\Delta\sigma_{\mathrm{sum}} = \sigma_0\left[\left(1 + \frac{\Delta\sigma_{gb}}{\sigma_0}\right)\left(1 + \frac{\Delta\sigma_{dis}}{\sigma_0}\right)\left(1 + \frac{\Delta\sigma_{spp}}{\sigma_0}\right) - 1\right] \tag{9}$$

where $\triangle\sigma_{sum}$ is the total strength increment, and σ_0 is the YS of specimens in group A.

Finally, using Eqs. (3), (7)–(9), the YS of the materials are calculated by substituting the parameters shown in Table 4, and the results are summarized in Table 5. It is worth noting that the calculated values are grossly consistent with the experimental data (138.8MPa by calculation and 123 MPa by experiment). $\Delta\sigma_{dis}$ is the predominant factor and takes 77.4% of the total strength increment. This result indicates that the dislocation strengthening exert a profound effect on the mechanical performance for group B. Meanwhile, the $\triangle\sigma_{gb}$ takes 26.8% of total strength enhancement in group B, implying that grain refinement contribution plays a second role and cannot be ignored. The SPPs strengthening, however, has a tiny effect on the total strength increment and can be neglect.

4.3. Correlation between microstructure and corrosion resistance

It has been revealed that the oxidation process of zirconium alloy is governed by the rate of oxygen ions diffusion through a dense protective layer to the oxide/matrix interface [41]. The different oxidation

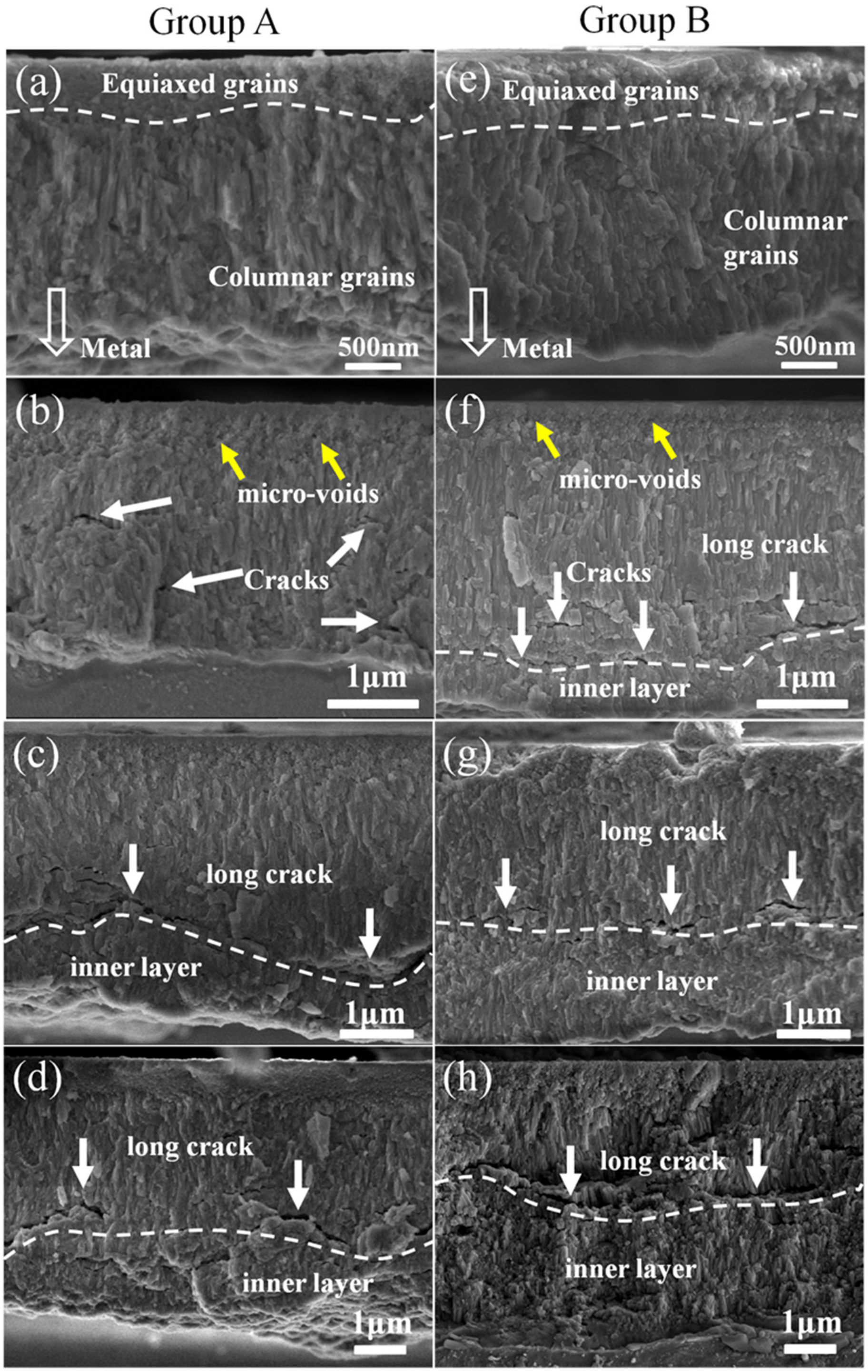

Fig. 11. SEM micrographs representative of the fracture surface of oxides formed for both groups. Panels (a)–(d) are the oxide morphologies for group A at exposure time of 100-day, 200-day, 260-day and 300-day, respectively. Panels (e)–(h) are the oxide morphologies for group B at exposure time of 100-day, 200-day, 260-day and 300-day, respectively.

rate is related to the microstructure of oxide formed on the surface of zirconium alloys [42,43]. As illustrated in Fig. 11, in the oxide films formed on the two groups, both large columnar grains and small equiaxed grains are observed. With up to 200 days, the oxide film in group B has more cracks, and some of these cracks inter-connected to form a longer crack, leading to the formation of two layers. Simultaneously, the corresponding weight gain of coupons in group B is higher than those in group A, indicative of a relatively worse corrosion resistance for group B. It is commonly accepted that the diffusion rate of oxygen anions in defects such as grain boundaries ($1.04 \times 10^{-16}\ \mathrm{m^2/s}$) [44] and dislocations is much higher than that in bulk ($9.32 \times 10^{-18}\ \mathrm{m^2/s}$) [45]. At the initial stage of oxidation, the corrosion rate in both groups is very high due to the direct contact of metal with water at high temperature. The oxide film is composed of small and equiaxed grains with high levels of micro-pores, as shown in Fig. 14. In group B, a predominant fraction of dislocation cells and subgrains were existed in the samples, therefore the diffusion rate would be relatively faster than in group A, and in consequence a higher oxidation

Table 3
Detailed information about the exposure time, oxide thickness for both groups.

Alloy	Exposure time (days)	Pre/post-transition	Oxide thickness (μm)		
			Total	Inner layer	Outer layer
Group A	100	Pre-transition	2.38–2.56	–	–
	200	Pre-transition	2.77–2.98	–	–
	260	Post-transition	3.49–3.77	0.66–0.79	2.83–2.98
	300	Post-transition	4.03–4.55	1.41–1.65	2.62–2.92
Group B	100	Pre-transition	2.26–2.56	–	–
	200	Post-transition	3.39–3.52	0.75–0.89	2.64–2.77
	260	Post-transition	4.90–5.41	1.72–2.11	2.88–3.10
	300	Post-transition	5.51–5.71	2.30–2.73	2.98–3.21

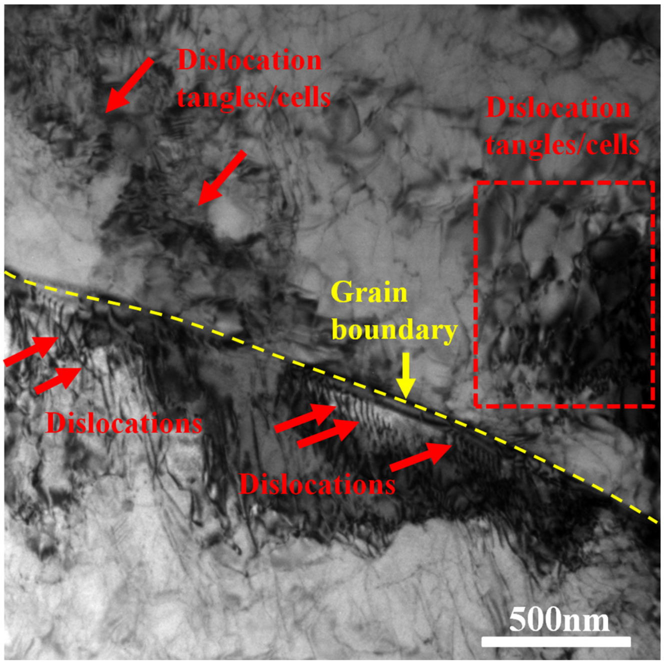

Fig. 12. TEM micrographs of samples in group B showing that high density of dislocations stack at the vicinity of the grain boundary and these dislocations tangle or form cells.

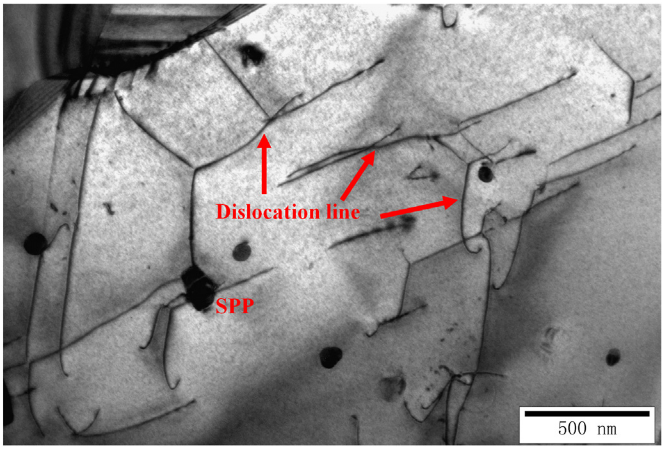

Fig. 13. High magnification TEM micrograph showing the pinning effect of SPPs against dislocations in specimens of group B.

Table 4
Parameters used in the calculation.

Parameter (unit)	Value	Ref.
k_{gb} (MPa $\mu m^{1/2}$)	200	[31]
b (nm)	0.323	[11]
G (GPa)	36.7	[25]
α	0.25	[33,34]
M	3.06/2.93	Tested
α'	0.8	[39]

Table 5
Calculated values of $\triangle\sigma_{gb}$, $\triangle\sigma_{dis}$, and $\triangle\sigma_{spp}$ of specimens in group B.

	Values (MPa)	Proportion in total $\triangle\sigma$ (%)
$\triangle\sigma_{gb}$	35.5	26.8
$\triangle\sigma_{dis}$	102.3	77.4
$\triangle\sigma_{spp}$	−5.7	−4.2
$\triangle\sigma_{sum}$	138.8	100

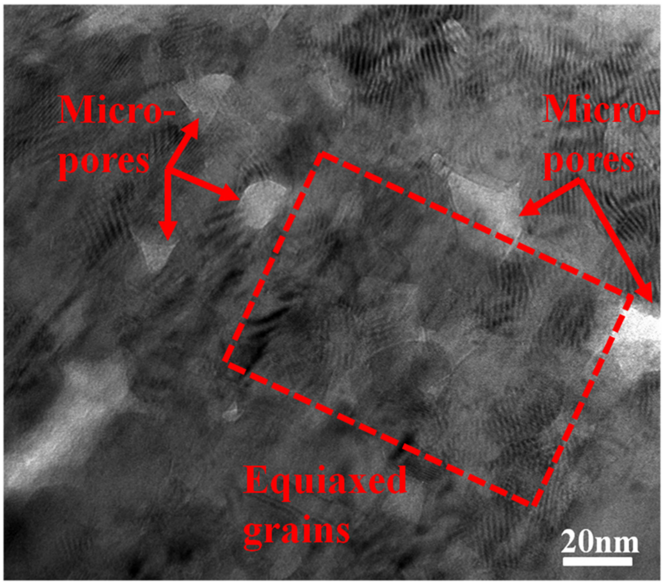

Fig. 14. High magnification TEM micrograph showing the outer part microstructure of oxide formed on group B at the initial stage of oxidation.

rate would achieved in group B at the early stage of oxidation. Although the weight gain of sample at the very beginning of oxidation is unknown, it still can be deduced by the first measure point of corrosion test. The corrosion rates (defined as the slope of the weight gain curve in Fig. 10) are respectively 3.75 and 4.64 for group A and B after 3 days exposure. As the oxide film thickens, the oxidation rate begins to slow owing to the formation of dense columnar grains in the inner oxide (Fig. 11a and e). This microstructure is confirmed to impede the diffusion of ions and could lead to the plateau region on the weight gain curve (Fig. 10). As the oxide film further thickens, some lateral cracks were formed in the oxide mainly parallel to the O/M interface (Fig. 11b and f). The oxide film on group B possesses more cracks, and some of them link together to form a long crack, leading to the delamination of oxide. A sudden increase of oxidation rate of group B is observed on the weight gain curve owing to the loss of protectiveness of oxide. The laying of oxide in group B indicates that the transition has occurred, while group A is still in the pre-transition stage. Water can penetrate the long crack to reach the O/M interface in group B and a new layer of oxide begins to form. The diffusion rate of oxide ions is significantly high at this time due to the high density of dislocations and much more sub-grains in group B. The transition time of oxide in group A is about

260 exposure days, and two layers are also examined (Fig. 11c). However, a relatively lower oxidation rate is measured in group A (0.258) after the first transition than that in group B (0.453). The completely recrystallized microstructure of group A contributes to the reduced corrosion rate after the first transition of oxidation.

On the other hand, a previous study on the Zr-2.5%Nb alloy has revealed that the initial stage of oxidation process involves lattice matching between the α-Zr matrix and oxide [46]. It is therefore predicted that the corrosion behavior will be affected by the matrix orientation. A recent investigation suggested that the oxidation process of a single-crystalline Ni-10at%Cr alloy in high temperature H_2O is the formation of vacancy clusters, and these vacancy clusters migrate and grow up by absorbing vacancies or merging with other vacancy clusters [47]. During the oxidation process, the high density of dislocations in group B will lead to large scale of lattice mismatch between matrix and oxide films, then lots of defects such as vacancies or dislocations will be produced in the oxide. Furthermore, the vacancy clusters formed by incorporating both Zr or O vacancies might absorb or interact with those vacancies or dislocations, then the vacancy clusters will gown up faster to form lots of micro-cavities, which further develop into more micro-cracks. These micro-cracks can act like the short circuit of the O ions diffusion paths, contributing to the faster corrosion rate for the specimens in group B.

To sum up, due to β-quenching and relatively low final annealing temperature, dislocation cells and sub-grains are dominant in the specimens of group B. These particular microstructures possess a relatively poor corrosion resistance, which can be ascribe to the higher O ion diffusion rate in defects and more vacancies or dislocations produced in the oxide.

5. Conclusions

Briefly, a Zr-Sn-Nb-Fe-Cu alloy is designed by two different heat treatments and the microstructure, tensile properties and corrosion resistance are investigated. Based on the results of the present investigation, the main conclusions can be drawn as follows:

(1) Compared with fully recrystallized samples in group A, a large scale of dislocation cells and sub-grains are dominant in group B, and the volume fraction and average size of SPPs in group B are relatively lower than those in group A. These discrepancies can attribute to the different heat treatments in two groups.
(2) The initial microstructures in two groups play an important role in the performance of tensile properties. For group A, a clear yielding with distinct upper and lower yield points in tensile curves is observed due to the complete recrystallized structure with little dislocations in group A. For group B, the direct work hardening behavior is obtained at the initial deformation due to the interaction of existing dislocations with GBs and SPPs.
(3) The enhancement of the YS in group B mainly originates from the combination of grain refinement and dislocation, and theoretical analysis shows that dislocation strengthening plays a significant role on the tensile property for group B.
(4) Autoclave corrosion test indicates that the samples in group B possess a relatively worse corrosion resistance than group A. It is attributed to the higher O ion diffusion rate in defects and more vacancies and dislocations generated in the oxide of group B.

Acknowledgements

The authors are grateful to the financial support of the National Natural Science Foundation of China (Grant No: U1602274, 51741108, 51371114, 51875349, 51501112), the Large Advanced Pressurized Water Reactor Major Project (No. 2017ZX06002005), the 111 Project (Grant No. B16032) and the Laboratory Innovative Research Program of Shanghai Jiao Tong University (Grant No. 17SJ-14).

Data availability

The raw data required to reproduce these findings are available upon request by email to the corresponding author: luweijie@sjtu.edu.cn.

References

[1] A. Garner, J. Hu, A. Harte, P. Frankel, C. Grovenor, S.L. Perez, M. Preuss, The effect of Sn concentration on oxide texture and microstructure formation in zirconium alloys, Acta Mater. 99 (2015) 259–272.
[2] N. Ni, D. Hudson, J. Wei, P. Wang, S.L. Perez, G.D.W. Smith, J.M. Sykes, S.S. Yardley, K.L. Moore, S. Lyon, R. Cottis, M. Preuss, C.R.M. Grovenor, How the crystallography and nanoscale chemistry of the metal/oxide interface develops during the aqueous oxidation of zirconium cladding alloys, Acta Mater. 60 (2012) 7132–7149.
[3] A. Garner, A. Gholinia, P. Frankel, M. Gass, I. MacLacren, M. Preuss, The microstructure and microtexture of zirconium oxide films studied by transmission electron backscatter diffraction and automated crystal orientation mapping with transmission electron microscopy, Acta Mater. 80 (2014) 159–171.
[4] A.T. Motta, Waterside corrosion in zirconium alloys, J. Miner. Met. Mater. Soc. 63 (2011) 59–63.
[5] A.T. Motta, A. Couet, R.J. Comstock, Corrosion of zirconium alloys used for nuclear fuel cladding, Annu. Rev. Mater. Res. 45 (1) (2015) 311–343.
[6] G.P. Sabol, ZIRLO™-an alloy development success, Proceeding of the 14th International Symposium on Zirconium in the Nuclear Industry, ASTM STP, 2005, pp. 3–24.
[7] J.P. Mardon, D. Charquet, J. Senevat, Influence of composition and fabrication process on out-of-pile and in-pile properties of M5 alloy, Proceeding of the 12th International Symposium on Zirconium in the Nuclear Industry, ASTM STP, 2000, pp. 505–524.
[8] A.V. Nikulina, Zirconium alloys in nuclear power engineering, Met. Sci. Heat Treat. 46 (2004) 458–462.
[9] J.M. Lee, S.I. Hong, Design and mechanical characterization of a Zr-Nb-O-P alloy, Mater. Des. 32 (2011) 4270–4277.
[10] D. Charquet, Phase constitution and steam corrosion resistance of binary Zr-S alloy, J. Nucl. Mater. 304 (2002) 246–248.
[11] H.L. Yang, S. Kano, Y. Matsukawa, Y.F. Li, J.J. Shen, Z.S. Zhao, F. Li, Y, Satoh, H. Abe, Study on recrystallization and correlated mechanical properties in Mo-modified Zr-Nb alloys, Mater. Sci. Eng. A 661 (2016) 9–18.
[12] S.K. Sahoo, V.D. Hiwarkar, I. Samajdar, G.K. Dey, D. Srivastav, R. Tiwari, S. Banerjee, Heterogeneous deformation in single-phase Zircaloy 2, Scr. Mater. 56 (2007) 963–966.
[13] L. Jiang, M.T. Pérez-Prado, P.A. Gruber, E. Arzt, O.A. Ruano, M.E. Kassner, Texture, microstructure and mechanical properties of equiaxed ultrafine-grained Zr fabricated by accumulative roll bonding, Acta Mater. 56 (2008) 1228–1242.
[14] B. Panicaud, D. Retraint, J.L. Grosseau-Poussard, L. Li, M. Guérain, P. Goudeau, N. Tamura, M. Kunz, Experimental and numerical study of the effects of a nanocrystallisation treatment on high-temperature oxidation of a zirconium alloy, Corros. Sci. 60 (2012) 224–230.
[15] M.Y. Yao, B.X. Zhou, Q. Li, W.Q. Liu, X. Geng, Y.P. Lu, A superior corrosion behavior of Zircaloy-4 in lithiated water at 360°C/18.6MPa by β-quenching, J. Nucl. Mater. 374 (2008) 197–203.
[16] L.Y. Chen, J.X. Li, Y. Zhang, L.C. Zhang, W.J. Lu, L.Q. Wang, L.F. Zhang, D. Zhang, Zr-Sn-Nb-Fe-Si-O alloy for fuel cladding candidate: processing, microstructure, corrosion resistance and tensile behavior, Corros. Sci. 100 (2015) 332–340.
[17] R.M. Langford, C. Clinton, In situ lift-out using a FIB-SEM system, Micron 35 (2004) 607–611.
[18] N. Bozzolo, G. Sawina, F. Gerspach, K. Sztwiertnia, A.D. Rollett, F. Wagner, Grain boundary character evolution during grain growth in a Zr alloy, Mater. Sci. Forum 558-559 (2007) 863–868.
[19] L.J. Chai, B.F. Luan, S.S. Gao, J.W. Chen, Q. Liu, Study of precipitate evolution and recrystallization of β-quenched Zr-Sn-Nb-Fe-Cr-Cu alloy during aging, J. Nucl. Mater. 427 (2012) 274–281.
[20] A.H. Cottrell, B.A. Bilby, Dislocation theory of yielding and strain ageing of iron, Proc. Phys. Soc. London, Sect. A 62 (1949) 49–62.
[21] Z. Wang, B. X. Zhou, B, Chen, W. Zhu, B. Wen, L. Wu, H. K. Tang, Z. Q. Fang, Q. Li, M. Y. Yao, In-situ oxidation and short-time corrosion investigation on dislocation during the generation and growth of ZrO_2, Corros. Sci. 122 (2017) 26–31.
[22] B.D.C. Bell, S.T. Murphy, P.A. Burr, R.J. Comstock, J.M. Partezana, R.W. Grimes, M.R. Wenman, The influence of alloying elements on the corrosion of Zr alloys, Corros. Sci. 105 (2016) 36–43.
[23] O.T. Woo, K. Tangri, Transformation characteristics of rapidly heated and quenched zircaloy-4-oxygen alloys, J. Nucl. Mater. 79 (1979) 83–94.
[24] R.A. Holt, The beta to alpha phase transformation in zircaloy-4, J. Nucl. Mater. 35 (1970) 322–334.
[25] L.J. Chai, B.F. Luan, D.P. Xiao, M. Zhang, K.L. Murty, Q. Liu, Microstructural textural evolution of commercially pure Zr sheet rolled at room and liquid nitrogen temperatures, Mater. Des. 85 (2015) 296–308.
[26] A. Cottrell, LXXXVI. A Note on the Portevin-Le Ghatelier Effect By A. H. 44 (1952), pp. 829–832.
[27] P.M. Anderson, J.P. Hirth, J. Lothe, Theory of Dislocations, 2nd ed., Krieger Publishing Company, New York, 1992, p. 424.

[28] Z.N. Yang, F.C. Zhang, Y.Y. Xiao, Z.G. Yan, Dynamic recovery: the explanation for strain-softening behaviour in Zr-2.3Nb alloy, Scr. Mater. 67 (2012) 959–962.

[29] C.Y. Yu, P.L. Sun, P.W. Kao, C.P. Chang, Mechanical properties of submicron-grained aluminum, Scr. Mater. 52 (2005) 359–363.

[30] N. Hansen, Hall-Petch relation and boundary strengthening, Scr. Mater. 51 (2004) 801–806.

[31] J.H. Keeler, The tensile characteristics of unalloyed zirconium at low and moderate temperatures, Trans. ASM 47 (1955) 157–185.

[32] Z.Y. Liang, Y.Z. Li, M.X. Huang, The respective hardening contributions of dislocations and twins to the flow stress of a twinning-induced plasticity steel, Scr. Mater. 112 (2016) 28–31.

[33] J.W. Dunlop, Y.J.M. Bréchet, L. Legras, Y. Estrin, Dislocation density-based modelling of plastic deformation of Zircaloy-4, Mater. Sci. Eng. A 443 (2007) 77–86.

[34] A. Sarkar, K.L. Murty, Microstructure-mechanical property correlation of cryo rolled Zircaloy-4, J. Nucl. Mater. 456 (2015) 287–291.

[35] E. Tenckhoff, The development of the deformation texture in Zirconium during rolling in sequential passes, Metall. Trans. A. 9 (1978) 1404–1412.

[36] D.A. Hughes, N. Hansen, Microstructure and strength of nickel at large strains, Acta Mater. 48 (2000) 2985–3004.

[37] P.A. Manohar, M. Ferry, T. Chandra, Five decades of the Zener equation, ISIJ Int. 38 (1998) 913–924.

[38] T. Nagasaka, H. Yoshida, K. Fukumoto, T. Yamamoto, H. Matsui, Mechanical properties of a high-purity Fe-9Cr-2W-0.1C model alloy for low-activation ferritic steels for fusion reactors, Mater. Trans. 1 (2000) 170–177 JIM.

[39] Y. Matsukawa, H.L. Yang, K. Saito, Y. Murakami, T. Maruyama, T. Iwai, K. Murakami, Y. Shinohara, T. Kido, T. Toyama, Z. Zhao, Y.F. Li, S. Kano, Y. Satoh, Y. Nagai, H. Abe, The effect of crystallographic mismatch on the obstacle strength of second phase precipitate particles in dispersion strengthening: bcc Nb particles and nanometric Nb clusters embedded in hcp Zr, Acta Mater. 102 (2016) 323–332.

[40] N. Ramakrishnan, An analytical study on strengthening of particulate reinforced metal matrix composites, Acta Mater. 44 (1996) 69–77.

[41] E.A. Garcia, Dynamical diffusion model to simulate the oxide crystallization and grain growth during oxidation of zirconium at 573 and 623 K, J. Nucl. Mater. 224 (1995) 299–304.

[42] H.J. Beie, A. Mitwalsky, F. Garzarolli, H. Ruhmann, H.J. Sell, Examinations of the corrosion mechanism of Zirconium alloys, Proceeding of the 10th International Symposium on Zirconium in the Nuclear Industry, ASTM STP 1245, 1993, pp. 615–643.

[43] D. Pêcheur, J. Godlewski, P. Billot, J. Thomazet, Microstructure of oxide films formed during the waterside corrosion of the Zircaloy-4 cladding in lithiated environment, Proceeding of the 11th International Symposium on Zirconium in the Nuclear Industry, ASTM STP 1295, 1995, pp. 94–113.

[44] I.G. Ritchie, A. Atrens, The diffusion of oxygen in alpha-zirconium, J. Nucl. Mater. 67 (1977) 254–264.

[45] B. Panicaud, J.L. Grosseau-Poussard, D. Retraint, M. Guérain, L. Li, On the mechanical effects of a nanocrystallisation treatment for ZrO_2 oxide films growing on a zirconium alloy, Corros. Sci. 68 (2013) 263–274.

[46] H. Li, M. Glavicic, J.A. Szpunar, A model of texture formation in ZrO2 films, Mater. Sci. Eng. A 366 (2004) 164–174.

[47] L.L. Luo, M. Su, P.F. Yan, L.F. Zou, D.K. Schreiber, D.R. Baer, Z.H. Zhu, G.W. Zhou, Y.T. Wang, S.M. Bruemmer, Z.J. Xu, C.M. Wang, Atomic origins of water-vapour-promoted alloy oxidation, Nat. Mater. 17 (2018) 514–518.